arXiv:1704.04551v1 [physics.flu-dyn] 14 Apr 2017

A parallel fluid solid coupling model using *LAMMPS* and *Palabos* based on the immersed boundary method

Jifu Tan[a], Talid Sinno[a], Scott Diamond[a,*]

[a] *Department of Chemical and Biomolecular Engineering*
University of Pennsylvania
Philadelphia, PA 19104, USA

Abstract

The study of viscous fluid flow coupled with rigid or deformable solids has many applications in biological and engineering problems, e.g., blood cell transport, drug delivery, and particulate flow. We developed a partitioned approach to solve this coupled Multiphysics problem. The fluid motion was solved by *Palabos* (Parallel Lattice Boltzmann Solver), while the solid displacement and deformation was simulated by *LAMMPS* (Large-scale Atomic/Molecular Massively Parallel Simulator). The coupling was achieved through the immersed boundary method (IBM). The code modeled both rigid and deformable solids exposed to flow. The code was validated with the classic problem of rigid ellipsoid particle orbit in shear flow and demonstrated essentially linear scaling over 16 cores. An example of the fluid-solid coupling was given for flexible filaments (drug carriers) transport in a flowing blood cell suspensions, highlighting the advantages and capabilities of the developed code.

Keywords: Lattice Boltzmann Method, Palabos, LAMMPS, Immersed Boundary Method, Parallel Computing

1. Introduction

Fluid flows containing solid particles are common in engineering and medicine, e.g., suspension flows [1], sedimentation[2], cell transport in blood flow [3, 4, 5, 6,

*Corresponding author, Email address: sld@seas.upenn.edu

7], and platelet deposition on blood vessel walls [8, 9, 10]. The dynamic behavior in such phenomena is complex due to interactions between individual particles as well as interactions between the particles and the surrounding fluid and bounding walls. Moreover, the presence of highly deformable particles, such as blood cells, vesicles and polymers, make it particularly challenging to accurately describe the dynamics in such systems. Understanding the interactions between the particulate components and the fluid is essential for optimized particulate design or detailed particulate flow behavior prediction, e.g., enhance particle mixing[11], fluid coking[12], drug carrier design[13, 4, 14], cell separation[15], and blood clotting[10, 16, 17].

The present paper is focused on blood flows containing a high concentration of deformable cells that are similar in size to the vessel diameter, thus requiring explicit consideration of the particle mechanics. Readers interested in the modeling of other classes of particulate flows, e.g., those relevant to industrial applications, are referred to other studies, e.g., ref. [18, 19, 20]. Numerous methods have been developed to model blood flows containing cells such as red blood cells and platelets. The boundary element method is an example of a very efficient technique for these types of flows[21, 22, 23] as it formulates boundary value problems as boundary integral equations. Thus, it only requires discretization of the surface rather than the volume. However, the boundary element method requires explicit knowledge of a fundamental or analytical solution of the differential equations, e.g., linear partial differential equations. Thus, it is limited to Stokes flow conditions. The Arbitrary-Lagrangian-Eulerian method (ALE) is another approach that has been used widely to model fluid-solid interactions[24, 25]. In ALE methods the fluid mesh boundary conforms to the solid boundaries on the interface, i.e., the nodes at the fluid-solid interfaces are shared. However, the ALE technique is computationally very expensive because repeated mesh generation is necessary for flows where particles experience large deformations (e.g., for red blood cells).

By contrast, non-conforming mesh methods eliminate the mesh regeneration step. In these methods, an Eulerian mesh is used for the fluid and a Lagrangian

mesh is used for the solid. These two meshes are independent, i.e., they do not share nodes across the interfaces. In this case, boundary conditions are applied through imposed constraints on the interfaces. The Immersed Boundary Method (IBM) is a popular example of a non-conforming mesh technique[26, 27]. Here, the velocity and force boundary conditions at the interfaces are imposed though interpolation functions that transfer velocities and forces across the domains. Consequently, the IBM approach may be regarded as an interface between two essentially separate simulators–one for evolving the particulate phase and the other for evolving the fluid. As we will show in this paper, the decoupled nature of the two components leads to a high degree of versatility in the context of software development. More generally, the present work represents an example of an emerging paradigm in multi-physics/multiscale modeling in which multiple existing (and independent) software packages are connected by a relatively simple interface to generate new functionality. Examples in the literature of such approaches include software packages for general fluid-solid coupling[28], sedimentation[29], atomic-continuum coupling[30], and fluid flow coupled with the discrete element method[19].

Another important aspect related to the implementation of methods for solving particulate flows is the portability to high performance computing (HPC) platforms so that large system sizes and long simulation times relevant to the phenomena of interest are accessible. An example of a reported HPC-enabled blood flow simulation is the work of [31], in which blood flow simulations in patient-specific coronary arteries at spatial resolutions ranging from the centimeter scale down to 10 μm were performed on 294,912 cores. In ref.[32], 2,500 deformable red blood cells in suspension under flow were simulated on IBM Blue Gene/P supercomputers. Additional examples include large-scale simulations of blood flow in the heart [33, 34, 35], cell separation in microfluidic flows[36, 15], and blood flow in the brain[37]. However, there are only a few parallel open sourced fluid solid coupling codes, such as the immersed boundary (IB) method with support for adaptive mesh refinement (AMR) *IBAMR*[38], the vascular flow simulation tool *SimVascular*[39, 40], the CFDEM project using computa-

tional fluid dynamics and discrete element methods[41, 19]. A general open source fluid solid coupling tool with versatile functionalities (e.g., deformable solids) and independent fluid and solid simulator is still missing.

In order to overcome challenges related to programming, model standardization, dissemination and sharing, and efficient implementation on parallel computing architectures, here we introduce a simple but effective implementation of the immersed boundary method for simulating deformable particulate flows using popular open source software. The fluid solver is based on the lattice Boltzmann method(LBM), chosen because of its efficient parallelization across multiple processor environments[42, 32]. LBM is a versatile fluid flow solver engine and has been used to model diverse situations, such as flows in porous media with complex geometries[43, 44] and multiphase flows[45, 46]. The solid particles in the fluids, particularly, the deformable blood cells are modeled as a coarse grained cell membrane model using particle based solid solver. In the present paper we employ a general LBM fluid solver *Palabos*[47, 48] and couple it with the *LAMMPS* software package [49] for describing particle dynamics. The reasons for building a large-scale parallel simulation tool for fluid-solid coupling based on widely used open source codes are evident. First, the implementation of a stable, efficient large-scale parallel solver for either fluid flow or particle dynamics is nontrivial, requiring training in scientific computing and software engineering. Both *Palabos* and *LAMMPS* are efficiently parallelized and clearly demonstrated by ample documentation and actively supported from large on-line communities:*LAMMPS* has an active mailing list that has hundreds questions and answers posted daily. These codes are also extensively validated by numerous examples and publications. Moreover, user-developers may easily extend the functionality of either package by implementing additional features, e.g., interaction potentials, integrators, fluid models, etc.

To the best of our knowledge, this is the first time *Palabos* has been coupled with *LAMMPS* in an immersed boundary method framework. The remainder of the paper is structured as follows. First, short introductions are provided in Section 2 describing the fluid solver (2.1), the solid solver (2.2), the immersed

boundary method (2.3), and the spatial decomposition for the coupling (2.4). Next in Section 3.1, a validation test and convergence study are presented for a single ellipsoid in a shear flow. The parallel performance of the IBM solver is studied in Section 3.2. Finally, an example of flexible filament transport in blood cell suspensions is described in Section 3.3, highlighting the advantages and capabilities of the new solver. Conclusions and discussions are provided in Section 4.

2. Methods

2.1. Lattice Boltzmann fluid solver: Palabos

Palabos is an open source computational fluid dynamics solver based on the lattice Boltzmann method (LBM). It is designed in C++ with parallel features using Message Passing Interface (MPI). It has been employed widely in both academic and industrial settings. The LBM has been used extensively in blood flow modeling [50, 51, 52, 10, 53]. Reviews of the underlying theory for the LBM can be found in the literature [54, 55, 56, 57]. LBM is usually considered as a second-order accurate method in space and time [58]. The fundamental quantity underpinning the LBM is the density distribution function $f_i(\boldsymbol{x}, t)$ in phase space $(\boldsymbol{x}, \vec{\boldsymbol{c}}_i)$, where t denotes the time and $\vec{\boldsymbol{c}}_i$ denotes the lattice velocity. The evolution of the density distribution function involves streaming and collision processes,

$$\underbrace{f_i(\boldsymbol{x} + \vec{\boldsymbol{c}}_i, t+1) - f_i(\boldsymbol{x}, t)}_{\text{streaming}} = \underbrace{\frac{1}{\tau}(f_i^{eq} - f_i(\boldsymbol{x}, t))}_{\text{BGK collision}} + F_i, \tag{1}$$

where the simplest Bhatnagar−Gross−Krook (BGK) scheme [59] is used for the collision term and F_i is the body force term that will be used to represent immersed cell boundaries[60]. The equilibrium distributionf_i^{eq} is given by

$$f_i^{eq} = w_i \rho \left(1 + \frac{\vec{\boldsymbol{c}}_i \cdot \vec{\boldsymbol{u}}}{c_s^2} + \frac{(\vec{\boldsymbol{c}}_i \cdot \vec{\boldsymbol{u}})^2}{2c_s^4} - \frac{\vec{\boldsymbol{u}}^2}{2c_s^2} \right), \tag{2}$$

where w_i are the weight coefficients and c_s is the speed of sound. The density ρ and velocity $\vec{\boldsymbol{u}}$ may be calculated as

$$\rho = \sum f_i, \quad \rho\vec{\boldsymbol{u}} = \sum f_i\vec{\boldsymbol{c}}_i + \frac{1}{2}\vec{\boldsymbol{g}}, \tag{3}$$

where $\vec{\boldsymbol{g}}$ is the external force density vector that is related to F_i as

$$F_i = (1 - \frac{1}{2\tau})w_i \left(\frac{\vec{\boldsymbol{c}}_i - \vec{\boldsymbol{u}}}{c_s^2} + \frac{\vec{\boldsymbol{c}}_i \cdot \vec{\boldsymbol{u}}}{c_s^4}\vec{\boldsymbol{c}}_i \right) \cdot \vec{\boldsymbol{g}}. \tag{4}$$

The fluid viscosity ν is related to the relaxation parameter τ as

$$\nu = c_s^2(\tau - 0.5) = \frac{\tau - 0.5}{3}. \tag{5}$$

In all LBM simulations reported in this paper, the fluid domain is discretized using a uniform D3Q19 lattice; see ref.[56]. The fluid density ρ, $\vec{\boldsymbol{u}}$ and density distribution function f_i are initialized at the equilibrium distribution calculated from Eqn.4 based on the initial fluid velocity. During each time step, streaming and collision steps are performed on f_i according to Eqn.1. Specifically, the f_i is translated in the direction of the discretized velocity vector $\vec{\boldsymbol{c}}_i$ during the streaming step; then, f_i is updated based on the equilibrium distribution, f_i^{eq}, the relaxation parameter, τ, and the force density, F_i, which is passed to the LBM from the immersed solid objects, e.g., blood cells.

2.2. Particle based solid solver: LAMMPS for deformable cells and particles

LAMMPS was originally designed as a molecular dynamics simulation tool[49]. In molecular dynamics, a potential function is defined to model the interactions between atoms. The force on each atom is calculated as the derivative of the potential with respect to the atomic coordinates and the atomic system motion is updated based on numerical integrations of Newton's 2nd law of motion. The *LAMMPS* package has now been extended to include a variety of additional dynamical engines, including peridynamics[61, 62], smooth particle hydrodynamics[63, 64], dissipative particle dynamics[65, 66], and stochastic rotation dynamics[67]. LIGGGHTS(*LAMMPS* improved for general granular and granular heat transfer simulations) is also an extension of *LAMMPS* for discrete

element method particle simulation[19]. Many predefined potentials, functions, and ODE integrators in *LAMMPS* make it extremely powerful for modeling atomic, soft matter[68], and biological systems[69, 8].

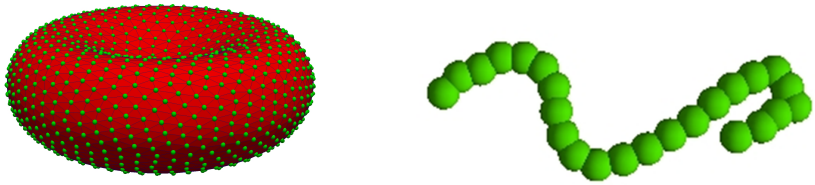

(a) A particle based coarse grained cell membrane model

(b) A polymer chain model

Figure 1: Models for a deformable red blood cell and a polymer chain implemented in *LAMMPS*: (a) a particle based coarse grained red blood cell membrane model that can bear stretching and bending. The particles on the cell membrane are interacting with potentials. (b) a particle connected polymer chain model with stretching and bending resistance.

A coarse-grained membrane model consisting of many interacting particles[70, 71, 72] is used to simulate red blood cells, as shown in Fig.1a. The membrane model can bear stretching and bending. Constraints to maintain the constant membrane surface area and enclosed cell volume are imposed through harmonic potentials. The viscosity ratio of cytoplasm over blood plasma is about 5. Here we treat the blood cell internal and external viscosity to be the same for saving computational cost. Readers interested in different viscosity models are referred to Ref.[5, 73, 74]. The potential function for a red blood cell (RBC) used in the current work is given by

$$U(\boldsymbol{X}_i) = U_{stretch} + U_{bending} + U_{area} + U_{volume}, \tag{6}$$

where the stretching energy $U_{stretch}$ is used to represent the cytoskeleton's resistance to deformation. The bending energy $U_{bending}$ represents the rigidity of the membrane bilayer and accompanying cytoskeleton. The last two terms are the constraints for maintaining constant membrane surface area and cell

volume. The stretching potential is given by:

$$U_{stretch} = \sum_{j \in 1...N_s} \left[\frac{k_B T l_m}{4p} \frac{3x_j^2 - 2x_j^3}{1 - x_j} + \frac{k_p}{l_j} \right], \tag{7}$$

where l_m is the maximum bond length, the jth bond length ratio is $x_j = l_j/l_m$. l_m was set to be 2 times the equilibrium bond length. N_s is the number of springs, p is the persistence length, k_B is the Boltzmann constant, T is the temperature, and k_p is the repulsive potential constant. Once p is specified, k_p may be found using the value of $x_j = 0.5$ at the equilibrium where the net force is zero.

The bending energy is defined as

$$U_{bending} = \sum_{j=1...N_s} k_b(1 - cos(\theta_j - \theta_0)), \tag{8}$$

where k_b is the bending constant and θ_j is the instantaneous angle formed by the two outward surface norms of two adjacent triangular meshes that share the same edge j. θ_0 is the corresponding equilibrium, or spontaneous, angle.

Constraints for constant membrane surface area and cell volume are imposed though area/volume dependent harmonic potentials,

$$U_{area} = \frac{k_g(A - A_0)^2}{2A_0} + \sum_{j=1...N_t} \frac{k_l(A_j - A_{j0})^2}{2A_{j0}}, \tag{9}$$

$$U_{volume} = \frac{k_v(V - V_0)^2}{2V_0}, \tag{10}$$

where k_g, k_l are the global and local area constraint constants, N_t is the number of triangular surfaces, A, A_0 are the instantaneous and spontaneous total surface area of the cell membrane, A_j, A_{j0} are the instantaneous and spontaneous surface area for the jth triangle surface, k_v is the volume constraint constant, and V, V_0 are the instantaneous and the equilibrium cell volume.

The parameters used in the coarse-grained membrane model can be related to membrane properties used in continuum model[72, 69], e.g., the shear modulus, μ_0, which is given by

$$\mu_0 = \frac{\sqrt{3}k_B T}{4pl_m x_0} \left[\frac{x_0}{2(1 - x_0)^3} - \frac{1}{4(1 - x_0)^2} + \frac{1}{4} \right] + \frac{3\sqrt{3}k_p}{4l_0^3}. \tag{11}$$

where $x_0 = l_0/l_m$ and l_0 is the bond length at equilibrium. Interested readers can refer to ref.[72, 69] for details.

For polymer particles, as shown in Fig.1b, the stretching energy is the same as Eqn.(7), while the bending energy is a harmonic function of the angle deviation,

$$U^p_{bending} = k^p_b(\theta_j - \theta_0)^2, \tag{12}$$

where the superscript p refers to polymer and the other variables are defined as in Eqn.(8).

To avoid the overlapping of the particles from different solid objects, e.g, cells, polymers, etc. a Morse potential was used for inter-particle interaction,

$$U_{morse} = D_0[e^{-2\alpha(r-r_0)} - 2e^{-\alpha(r-r_0)}], \quad r < r_c. \tag{13}$$

where D_0 is the energy scale, α controls the width of the potential, r is the distance between particles from different solid objects, r_0 is the equilibrium distance, r_c is the cutoff distance.

All the parameters used in the simulation are listed in Table 2.

2.3. Fluid-solid coupling: the immersed boundary method

The immersed boundary method (IBM) was used to model the coupling between fluid and solid. The combination of LBM and IBM was first used to model fluid-particle interaction problems in ref. [75]. Details of the immersed boundary method formulation may be found in refs. [26, 27, 75]. Briefly, the solid velocity at each particle position is obtained through velocity interpolation from local fluid nodes, while fluid forces are obtained by spreading the local solid forces. Specifically, for an immersed solid with coordinates $\boldsymbol{X}$, the velocity $\boldsymbol{U}(\boldsymbol{X}, t)$ is interpolated from the local fluid velocity $\boldsymbol{u}(\boldsymbol{x}, t)$, while the solid force, $\boldsymbol{F}(\boldsymbol{X}, t)$, calculated from Eqn.6 is spread out into the local fluid grid points as a force density $\boldsymbol{f}(\boldsymbol{x}, t)$:

$$\boldsymbol{U}(\boldsymbol{X}, t) = \int \boldsymbol{u}(\boldsymbol{x}, t)\delta(\boldsymbol{x} - \boldsymbol{X})d\boldsymbol{x}, \tag{14}$$

$$\boldsymbol{f}(\boldsymbol{x},t) = \int \boldsymbol{F}(\boldsymbol{X},t)\delta(\boldsymbol{x}-\boldsymbol{X})d\boldsymbol{X}, \tag{15}$$

where $\delta(\boldsymbol{x})$ is the delta function. In a typical numerical implementation in three dimensions, $\delta(\boldsymbol{x})$ is constructed as the product of one-dimensional functions, i.e., $\delta(\boldsymbol{x}) = \phi(x)\phi(y)\phi(z)$ with $\phi(r)$ defined as

$$\phi(r) = \begin{cases} 0, & \text{otherwise} \\ \frac{1}{4}\left(1 + cos\left(\frac{\pi r}{2}\right)\right), & |r| \leq 2, \end{cases} \tag{16}$$

where r is the distance between solid particles and fluid nodes. Different choices of the interpolation function influence the coupling accuracy, the influence range of the solid particles on the fluid, and the computational cost [76, 77]. Schematic representations of the velocity interpolation and force spreading process used in the present implementation are shown in Fig.2.

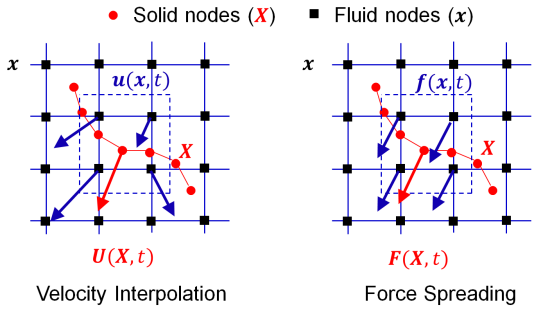

Figure 2: An illustration of the fluid-solid coupling through the immersed boundary method. The solid velocity for each particle, $\boldsymbol{U}(\boldsymbol{X},t)$, is interpolated from the local fluid velocities, $\boldsymbol{u}(\boldsymbol{x},t)$, while the solid force at each particle $\boldsymbol{F}(\boldsymbol{X},t)$ is spread out onto the local fluid nodes, $\boldsymbol{f}(\boldsymbol{x},t)$. The influence range of the central solid particle on fluid is shown in dashed rectangles.

The coupling strategy described above becomes numerically unstable for rigid objects. In such situations, a different fluid-solid interaction (FSI) approach must be applied [78, 79]. In the present IBM formulation for rigid particles, the FSI force on each particle is used to assemble the total force and torque on the whole rigid body. The translation and rotation of the rigid object

are then updated based on Newton's 2nd law of motion. The FSI force can be expressed as:

$$f^{FSI}(\boldsymbol{X},t) = \rho_f(\boldsymbol{u}(\boldsymbol{X},t) - \boldsymbol{U}(\boldsymbol{X},t))/\delta t, \tag{17}$$

where ρ_f is the fluid density, $\boldsymbol{u}(\boldsymbol{X},t)$ is the fluid velocity at the solid boundary node $\boldsymbol{X}$, which has to be obtained through interpolation by Eqn.(14). $\boldsymbol{U}(\boldsymbol{X},t)$ is the solid nodal velocity. The idea behind Eqn.(17) is that the local fluid particles with incoming velocity $\boldsymbol{u}(\boldsymbol{X},t)$ will collide with the solid boundary with outgoing velocity $\boldsymbol{U}(\boldsymbol{X},t)$. The FSI force is the change of the momentum divided by the collision time δt. Other approaches have been proposed to model rigid objects in IBM, e.g., a virtual boundary formulation was used in ref.[80].

2.4. Spatial decomposition for fluid-solid coupling

Spatial decomposition is adopted by both *Palabos* and *LAMMPS* for parallel computing. In our fluid-solid coupling approach, the same spatial decomposition was applied to both the fluid and the solid so that the coupling can be effectively handled by the same compute core for a given region. Consistent spatial decomposition for the two domains ensures that individual processors have access to both the fluid grid points and solid particles within the same sub-domain. An illustration of the partitioning process is shown in Fig.3, where the whole fluid-solid system is partitioned onto 8 compute cores. Ghost layers near the boundaries of each sub-domain are used for communication between neighboring cores. This approach may not be optimal for a system where solid particles are highly heterogeneously distributed across the entire domain. However, for most cases of interest the distribution of solid particles is quite homogeneous, and in any case, the majority of the computation is dedicated to the fluid solver. The issue of load optimization for heterogeneous systems is deferred to future work.

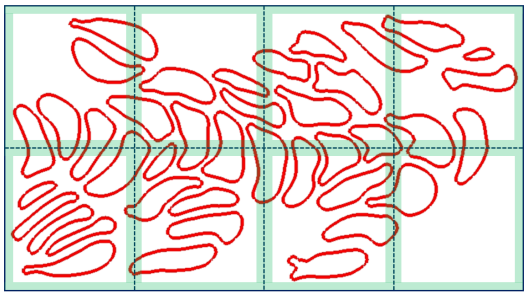

Figure 3: Spatial decomposition for parallel computing for fluid solid coupling. The blood flow with cells (red lines) was divided into multiple regions. One processor was assigned to each region to calculate the both fluid and solid motions within the region, thus, the coupling between fluid and solid within the region is local to the processor. On the interface between processors, ghost layers (green stripe) were used for communication for both fluid and solid independently. An example of 8 processors were used for the task partition in the figure.

The FSI coupling algorithm consists almost entirely of two routines to carry out velocity interpolation and force spreading functions. As mentioned above the fluid solver usually represents the bulk of the computational demand because the solid fraction is usually quite small. Based on this intrisic asymmetry, we employed *Palabos* as the driving code, while *LAMMPS* was called as an external library. To fully access all the members(e.g., particle positions, velocities, forces, etc.) from *LAMMPS*, a pointer to *LAMMPS* was used and passed to the two interpolation functions. An outline of the functions implemented in our IBM algorithm is shown in List1.

List 1: function declarations for IBM

```
template<typename T,template<typename U> class Descriptor>
void interpolateVelocity3D(MultiBlockLattice3D<T,Descriptor>
      &lattice,LAMMPSWrapper &wrapper);

template<typename T,template<typename U> class Descriptor>
void spreadForce3D(MultiBlockLattice3D<T,Descriptor>
     &lattice,LAMMPSWrapper &wrapper);
```

where *lattice* is the structure used in *Palabos* to store the population distri-

bution functions for the LBM, while *wrapper* is a pointer to an instance of *LAMMPS*. The advantage of the IBM in terms of software development is that only two functions are needed to couple a fluid solver to a solid solver. Our IBM implementation therefore only requires a few hundred lines of code beyond what is implicitly contained in the *Palabos* and *LAMMPS* packages.

3. Results

3.1. Validation: Ellipsoid in shear flow

To validate our IBM implementation, we considered the trajectory of a rigid ellipsoid in a shear flow in Stokes flow regime, commonly referred to as the Jeffery's orbit[81], where the rotation angle of the ellipsoid, θ, satisfies

$$tan\theta = \frac{b}{a} tan \frac{ab\gamma t}{a^2 + b^2}, \tag{18}$$

where θ is the angle formed by the major axis of the ellipsoid and the shear flow direction, a, b are the major and minor semi-axis lengths, γ is the shear rate, and t is the time. A 2D illustration of the ellipsoid is shown in Fig.4–the third semi-axis length is assumed to be the same as b.

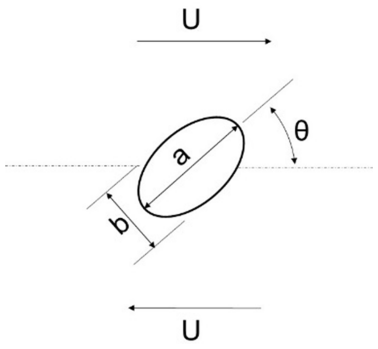

Figure 4: An illustration of an ellipsoid in a shear flow. a, b are the major and minor semi-axis lengths, and U is the magnitude of the velocities applied at the top and bottom plates. The distance between the top and bottom parallel plate is H, giving a shear rate $\gamma = 2U/H$.

An ellipsoid with semi-axis lengths $a = 6, b = c = 4.5$ was placed at the center of a channel with height $H = 60$. The top and bottom velocities were

set to $U = 0.01$ and a viscosity of $\nu = 1/6$ was prescribed. These parameters give a shear rate $\gamma = 0.00033$ and a Reynolds number of $Re = aU/\nu = 0.36$ to approximate Stokes flow. The IBM numerical result for the orientation angle θ and the analytical solution given by Eqn.(18) are plotted in Fig.5. The agreement is good, validating the FSI coupling. Shown in Fig.6 is the relative error, defined as $\frac{|\theta_{sim} - \theta_{the}|}{\theta_{the}}$ where θ_{sim} is the simulation data and θ_{the} is the theoretical data from Eqn.18. The relative error is seen to oscillate with the period of the ellipsoid and is, on average, constant at about 2.62%.

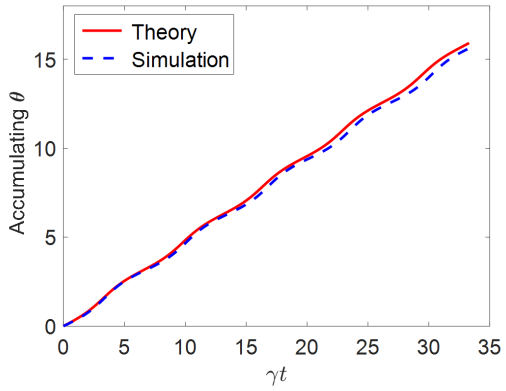

Figure 5: The comparison between Jeffery's orbit given by Eqn.18 and numerical results simulated by the fluid solid coupling code

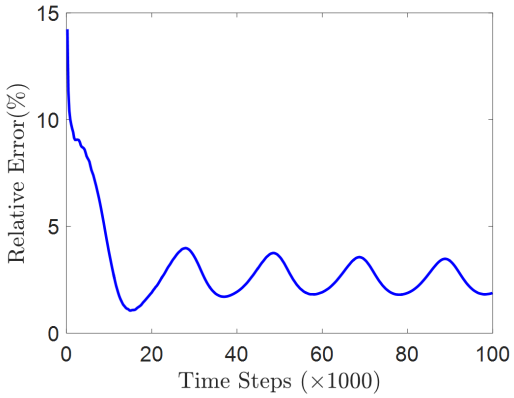

Figure 6: The relative error of the ellipsoid rotation angle θ calculated based on the fluid solid coupling at $Re = 0.36$. The fluid grid was $60 \times 60 \times 30$.

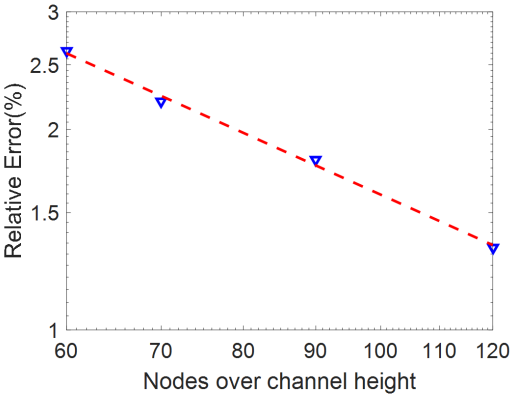

Figure 7: The convergence for the fluid solid coupling at $Re = 0.36$ with different grid resolutions. The convergence rate is nearly linear to the grid spacing, as indicated by the dashed line. The relative error $\epsilon \propto N^{-0.96}$ where N is the grid resolution over channel height H.

As expected, the relative error ϵ is a power function of the fluid grid resolution N–Fig. 7 shows that the relative error scales as the grid spacing following $\epsilon \propto N^{-0.96}$.

3.2. Scalability: Parallel performance

The parallelization performance of the IBM code was examined using a benchmark simulation of red blood cells flowing in a rectangular box, see Fig.8.

The fluid domain was discretized into a total of 10,240,000 grid points ($50 \times 50 \times 4,096$) with one inlet and one outlet and 4 nonslip side walls. The Reynold's number defined on the channel width was 0.05. The solid phase consisted of 208 red blood cells, discretized into $133,536$ particles connected by $399,360$ bonds, $266,240$ angles, and $399,360$ dihedrals in total. The cells were initially uniformly distributed in the flow domain. The pair-wise inter-particle potential was deactivated because of the large inter-cell spacing, as shown in Fig.8. The IBM simulations were executed on 2 AMD Opteron 8-core 6128 processors with a clock speed of 2.0 GHz and the CPU time for 100 time steps was recorded. A ghost layer with thickness of three fluid lattice spacings was employed for inter-processor communication within the fluid solver. The ghost cutoff distance for *LAMMPS* was set to 1.5 times the LBM lattice spacing. The domain was decomposed into a linear array of segments along the length of the channel. The execution times, averaged over 3 independent runs, for the fluid-solid coupling simulation, the fluid solver component (*Palabos*) and the solid solver component (*LAMMPS*) are plotted in Fig.9. All three exhibit linear scaling with respect to the number of cores. The execution time was found to scale with the number of processors according to a power law function of the form, $T \propto N^c$, with exponents $c = [-0.8945, -0.9512, -0.9579]$ for the fluid solid coupling simulation, *Palabos*, and *LAMMPS* components, respectively. These results demonstrate that each of the components of the IBM parallelize efficiently.

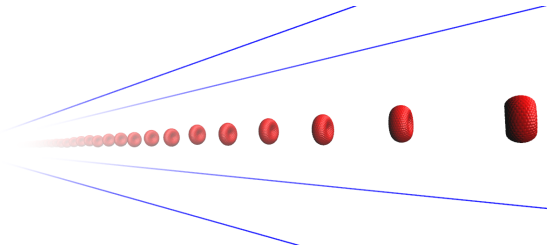

Figure 8: Red blood cells (red particles) flowing in a rectangular box for performance testing. The simulation box size is $50\mu m \times 50\mu m \times 4,096\mu m$. Only 4 parallel edges of the box are shown as it is too long to be visualized in full length.

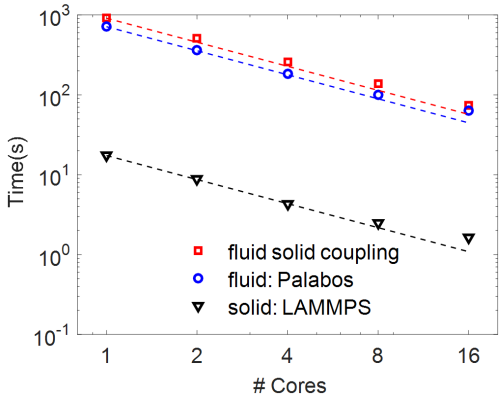

Figure 9: Comparison of the performance between the fluid solid coupling simulation, the fluid solver (*Palabos*) and the solid solver (*LAMMPS*). The dashed lines showed theoretical cases for perfect linear scaling.

The parallelization performance was analyzed further by defining an efficiency parameter, γ of the form

$$\gamma(N) = \frac{t_1}{N \times t_N} \times 100\%, \tag{19}$$

where t_1 is the time to finish the task on a single core, while t_N is the time to finish the same task on N cores. The scaling efficiency γ was plotted in Fig.10 and demonstrates that the coupling algorithm scales at least as well as *LAMMPS* and *Palabos*, both of which are highly optimized for parallel efficiency.

The scaling efficiency was found to depend strongly on the computer hardware. For example, significantly less parallel efficiency was obtained on another computer with Intel Xeon E5630 2.53 GHz processors (16 cores in total). While we did not study architecture dependence in more detail here, these results suggest that further work is needed to assess architecture-dependent performance issues. Finally, we note that the ghost layer thickness also influenced the performance of the IBM code. In the present study we used 3 layers of lattice points, while other studies have employed linear interpolation kernels that only require a single layer of lattice points for the communication layer[82].

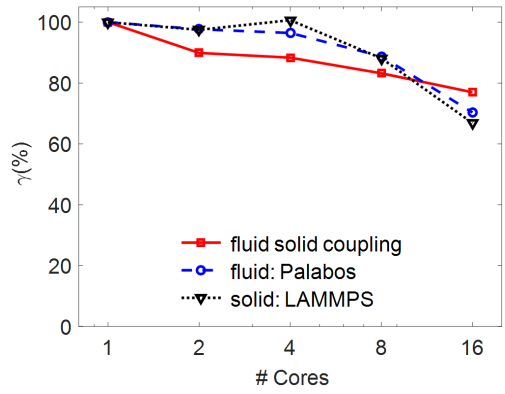

Figure 10: The strong scaling efficiency of the code over different number of processors

The extra computational time induced by the coupling can be estimated as the difference between the total execution time for the coupled code and the sum of individual fluid and solid computing times. On average, the extra computational time required for the information exchange between the fluid and solid solvers was about 6.9%, e.g., time spent on the two coupling functions: interpolateVelocity3D and spreadForce3D. The computational time for the two coupling functions expressed in terms of the percentage over the total CPU time is shown in Table 1. The function interpolateVelocity3D cost about 5.13% on average, while function spreadForce3D cost about 1.66%.

ID	Functions	CPU time (%)				
		p1	p2	p4	p8	p16
t_1	interpolateVelocity3D	4.5	5.21	7.13	6.98	1.84
t_2	spreadForce3D	1.82	1.67	1.59	1.75	1.45
$t_1 + t_2$		6.32	6.88	8.72	8.73	3.29

Table 1: The percentage of CPU time for the coupling functions.

3.3. Case Study: Transport of flexible filaments in flowing red blood cell suspensions

Next, the validated IBM code was applied to a problem relevant to drug carrier delivery in microcirculation flows to demonstrate its capabilities in a more complex setting. This is a multi-physics modeling problem as it involves fluid flow, large cell deformations, and polymer transport[6, 4, 83, 4, 7]. Of particular interest is the observation that particles with different sizes, shapes, or flexibility can exhibit distinct transport properties in the blood stream. For example, long flexible filaments persist in the circulation up to one week after intravenous injection in rodent models. This is about ten times longer than for spherical counterparts[84]. The flexibility and filament length may influence transport and contribute to the anomalously long circulation time.

We simulated filament transport in tube flow of red blood cell suspensions and analyzed filament migration, apparent size, spatial distribution, and dispersion rate. The fluid domain was represented by a cylindrical tube with diameter of $30\mu m$ and length $50\mu m$, as shown in Fig.11. No-slip conditions were applied at the cylinder wall while periodic boundary conditions were applied at the inlet and outlet. The relaxation time was set to $\tau = 1$ giving a dimensionless kinetic viscosity of 1/6. The LBM lattice spacing, dx, was fixed at $0.33\mu m$, the time step was set to $dt = 1.82 \times 10^{-8}s$. One hundred red blood cells were placed in the domain corresponding to a cell concentration of about 27%, which is within the physiological range[85]. Each cell was described by 1,320 surface nodes, 3,954 stretching bonds, 2,636 area segments, and 3,954 bending angles. A force density was applied to drive the flow such that the shear rate at the wall was $1000s^{-1}$ without the red blood cells. The actual wall shear rate was less as the blood cell component reduces the flow rate. A total of 156 filaments were then introduced at one end of the cylinder as shown in Fig.11. Each filament was a polymer chain modeled as beads connected by stretching and bending springs. Different lengths ($2\mu m$ and $8\mu m$) and different bending stiffnesses (4.1×10^{-20} J, or about $10k_BT$, and 4.1×10^{-18} J, corresponding to about $1000k_BT$) were used to study the size and stiffness effect on filament transport in red blood cell

suspensions.

The parameters used in the simulations are listed in Table.2. The corresponding shear modulus for red blood cell membranes was $\mu_0 = 6\mu N/m$ based on Eqn.11.

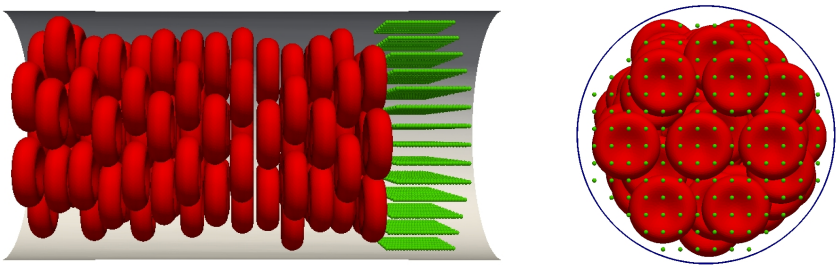

(a) Front view (b) Side view

Figure 11: Initial positions for the blood cells and filaments. The cells were randomly distributed in the blood vessel, while the filaments were uniformly distributed in one end of the vessel.

Red blood cells				
$k_BT/p(N)$	$k_b(J)$	$k_g(N/m)$	$k_l(N/m)$	$k_v(N/m^2)$
1×10^{-12}	2.3×10^{-19}	2.1×10^{-4}	2.1×10^{-4}	2.2
Filaments				
$k_BT/p(N)$	$k_p(J)$	$k_b(J)$	$l_0(\mu m)$	$\theta_0(^\circ)$
1.36×10^{-12}	1.7×10^{-12}	$[4.1, 410] \times 10^{-20}$	0.33	180
Morse potential				
$D_0(J)$	α	$r_0(\mu m)$	$r_c(\mu m)$	
1.2×10^{-18}	0.5	0.66	0.66	

Table 2: Simulation parameters used for the particle transport in blood flow. The shear modulus for the cell $\mu_0 = 6\mu N/m$. The Morse potential was used to avoid the filament-cell and cell-cell overlapping.

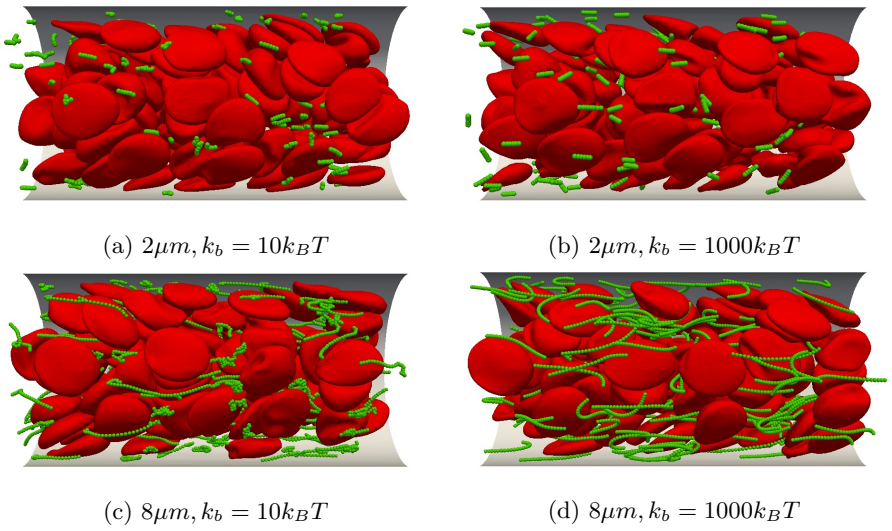

(a) $2\mu m, k_b = 10k_BT$ (b) $2\mu m, k_b = 1000k_BT$

(c) $8\mu m, k_b = 10k_BT$ (d) $8\mu m, k_b = 1000k_BT$

Figure 12: Snapshots of the simulations of filaments (green) mixing with blood cell suspensions (red) at 8×10^6 time steps. $2\mu m$ filaments with bending stiffness $10k_BT$ (a) and $1000k_BT$ (b); $8\mu m$ filaments with bending stiffness $10k_BT$ (c) and $1000k_BT$ (d). Half of the vessel wall was also shown in the figure.

Simulation snapshots at 8×10^6 time steps are shown in Fig.12 for cases with different filament size and flexibility. Different configurations are observed for filaments with different stiffnesses. The stiffer filaments were generally straight when the length was $2\mu m$, and exhibited a small amount of curvature for $8\mu m$, see Fig.12b and 12d. By contrast, the more flexible filaments exhibited highly bent or coiled shapes, particularly for the $8\mu m$ filaments, see Fig.12a and 12c. The apparent filament size, defined as the maximum extent for the filaments, is shown in Table.3. The apparent size for stiffer filaments was very close to the actual contour length, while the apparent size for flexible filaments was smaller than the actual contour length, due to the bending and coiling of the filaments.

The average radial position and the mean square displacement (MSD) for the filaments are plotted in Fig.13 and Fig.13a. Filament migration towards the vessel wall was observed for all filament types but was found to be reduced for the longer, more flexible filaments. The dispersion rate, defined as the

contour size(μm)	1.66		7.92	
stiffness(k_b/k_BT)	10	1000	10	1000
apparent size(μm)	1.57 ± 0.31	1.67 ± 0.01	5.76 ± 2.4	7.89 ± 1.92
dispersion rate($\times 10^{-11} m^2/s$)	9.76	8.64	6.26	7.26

Table 3: The apparent size and dispersion rate of the filaments in the blood flow with cells. The apparent size of the filaments were smaller than the actual contour length due to the bending and coiling. The dispersion rate was in the order of $10^{-11} m^2/s$, which was about 2 orders-of-magnitude larger than thermal diffusion for microparticles.

slope of the MSD curve, is shown in Table 3. The dispersion rates are all of the order of $10^{-11} m^2/s$, which is about 2 orders-of-magnitude larger than the background thermal diffusion expected for particles of this size. This finding is consistent with other observations for small particles in blood suspensions, such as platelets[23, 86, 87], particles[4, 13] and experimental measurements for microparticles[88].

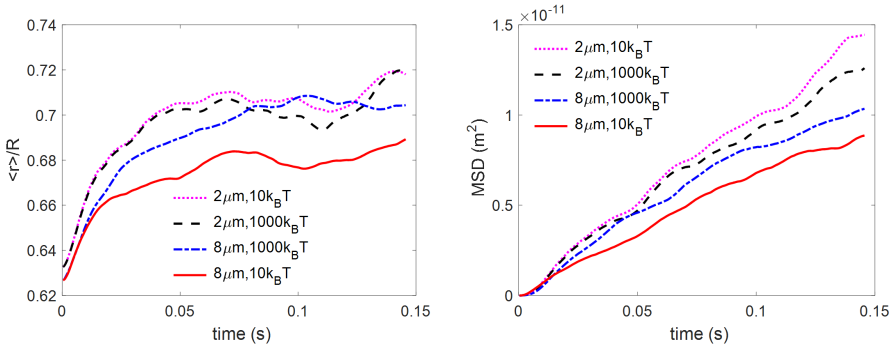

(a) Normalized radial position (b) Mean Square Displacement

Figure 13: (a) The averaged filament center position normalized with the vessel radius $R = 15\mu m$. (b) The mean square displacement for the filaments transported with the blood cells.

The fraction of filaments present in the $3\mu m$ cell-free layer near the vessel wall is shown in Fig.14. The fraction of the $2\mu m$ filaments increases approximately monotonically from 28% (the baseline value assuming a uniform distribution) to 46.3% for soft filaments, and to 43.8% for stiff filaments. In other words, the

migration of smaller filaments toward the cell-free layer is not sensitive to the stiffness. However, for $8\mu m$ filaments, the flexible ones exhibited a transient peak fraction of 50.2% in the cell-free layer, then decreasing to 37.8%, while the rigid ones maintain a cell-free layer fraction of 46%. These results suggest that soft filaments can traverse red blood cell layers relatively easily by coiling, while the more rigid filaments are hindered by their size.

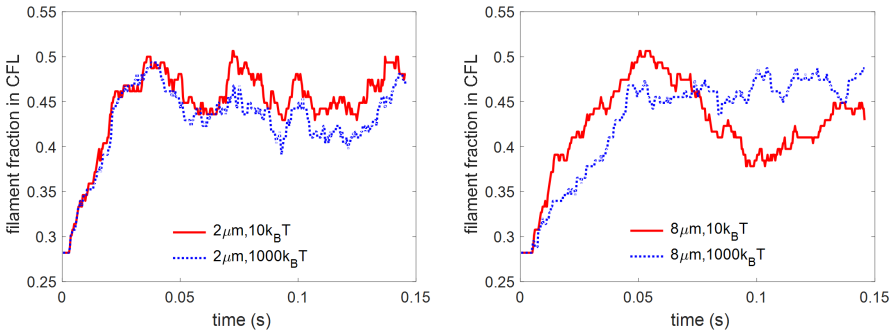

(a) $2\mu m$ (b) $8\mu m$

Figure 14: The fraction of the filaments in the cell free layer of the blood vessel. The cell free layer was defined as a $3\mu m$ thickness layer next to the vessel wall. (a) $2\mu m$; (b)$8\mu m$.

Several filament trajectories in flowing blood cell suspension are shown in Fig.15 to illustrate the filament traversing process. Soft filaments can traverse blood cell layers from the core region ($r/R < 0.8$) to the cell free layer ($r/R > 0.8$) and from the cell free layer to the core region. However, stiff filaments showed less migration toward the core region. Interestingly, the filaments also showed different shapes at $t = 0.088s$ when their trajectory started to diverge. The soft ones can coil themselves into smaller size to traverse through the torturous gaps formed by the red blood cells, see Fig.16a. Whereas, the stiff ones would require more energy to deflect their shape to pass through the torturous gaps, as indicated from Fig.16b. Thus, the migration from cell free layer to the core region for stiff ones is limited. These results indicate that flexibility influences long filament transport in flowing blood cell suspensions.

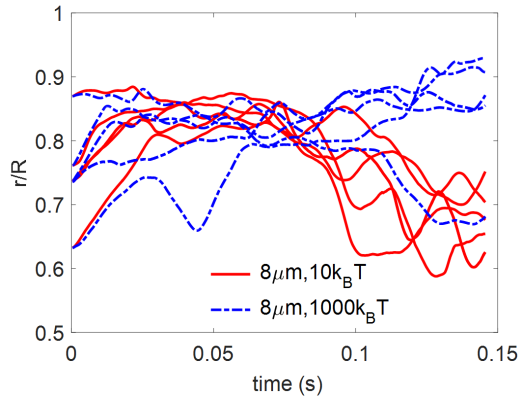

Figure 15: The trajectories of five filaments with different flexibility in the blood cell suspensions. Soft filaments traversed across cell layers relatively easier than more rigid ones.

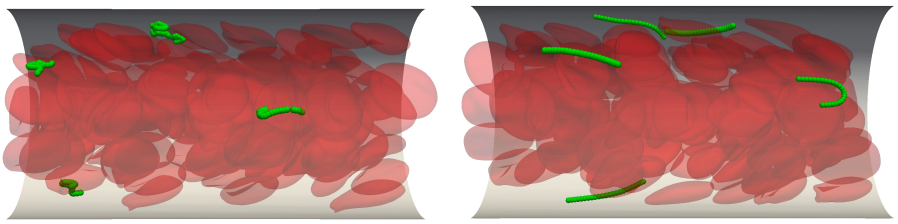

(a) $8\mu m, 10k_BT$ (b) $8\mu m, 1000k_BT$

Figure 16: Representative shapes of the $8\mu m$ filaments with different flexibility in flowing blood cell suspensions. Soft filaments showed smaller apparent size compared with more rigid ones. (a) $10k_BT$; (b)$1000k_BT$.

4. Conclusions

We introduced an efficient implementation of the Immersed Boundary Method by coupling a Lattice Boltzmann fluid solver with a particle-based solid solver using open source codes, namely *Palabos* and *LAMMPS*, respectively. The coupling was achieved by a simple interface that only requires a few hundred lines of code, dramatically reducing software development time, increasing robustness and facilitating transferability. The coupling is demonstrated to be computationally efficient, requiring only about a 6.9% increase in the computational cost

beyond what is required for executing fluid and solid solvers. The IBM code also is shown to scale on parallel architectures as well as the intrinsic scaling of *Palabos* and *LAMMPS*, at least for moderate numbers of cores. Further work will be required to assess parallelization efficiency in massively parallel environments.

The validated IBM code was used to analyze polymer filament transport in red blood cell flows; such filaments are of interest for drug delivery applications. Simulations demonstrated how filament flexibility reduce the effective size of filament, so that flexible filaments can traverse through the blood cell suspensions easier than stiffer ones. These results highlight the complex physics that may underlie the long circulation time found for such particles in rodents [84].

5. Acknowledgment

This work was supported by NIH 1U01HL131053-01A1.

References

[1] P. R. Nott, J. F. Brady, Pressure-driven flow of suspensions: simulation and theory, Journal of Fluid Mechanics 275 (1994) 157–199.

[2] J. Feng, H. H. Hu, D. D. Joseph, Direct simulation of initial value problems for the motion of solid bodies in a newtonian fluid part 1. sedimentation, Journal of Fluid Mechanics 261 (1994) 95–134.

[3] D. A. Fedosov, B. Caswell, A. S. Popel, G. E. Karniadakis, Blood flow and cell-free layer in microvessels, Microcirculation 17 (8) (2010) 615–628.

[4] K. Vahidkhah, P. Bagchi, Microparticle shape effects on margination, near-wall dynamics and adhesion in a three-dimensional simulation of red blood cell suspension, Soft Matter 11 (11) (2015) 2097–2109.

[5] S. K. Doddi, P. Bagchi, Lateral migration of a capsule in a plane poiseuille flow in a channel, International Journal of Multiphase Flow 34 (10) (2008) 966–986.

[6] K. Sinha, M. D. Graham, Shape-mediated margination and demargination in flowing multicomponent suspensions of deformable capsules, Soft matter 12 (6) (2016) 1683–1700.

[7] J. Tan, A. Thomas, Y. Liu, Influence of red blood cells on nanoparticle targeted delivery in microcirculation, Soft matter 8 (6) (2012) 1934–1946.

[8] I. V. Pivkin, P. D. Richardson, G. Karniadakis, Blood flow velocity effects and role of activation delay time on growth and form of platelet thrombi, Proceedings of the National Academy of Sciences 103 (46) (2006) 17164–17169.

[9] A. L. Fogelson, R. D. Guy, Immersed-boundary-type models of intravascular platelet aggregation, Computer methods in applied mechanics and engineering 197 (25) (2008) 2087–2104.

[10] Y. Lu, M. Y. Lee, S. Zhu, T. Sinno, S. L. Diamond, Multiscale simulation of thrombus growth and vessel occlusion triggered by collagen/tissue factor using a data-driven model of combinatorial platelet signalling, Mathematical Medicine and Biology (2016) dqw015.

[11] Y. Tsuji, T. Kawaguchi, T. Tanaka, Discrete particle simulation of two-dimensional fluidized bed, Powder technology 77 (1) (1993) 79–87.

[12] J. Gao, J. Chang, C. Xu, X. Lan, Y. Yang, Cfd simulation of gas solid flow in fcc strippers, Chemical Engineering Science 63 (7) (2008) 1827–1841.

[13] K. Müller, D. A. Fedosov, G. Gompper, Understanding particle margination in blood flow–a step toward optimized drug delivery systems, Medical engineering & physics 38 (1) (2016) 2–10.

[14] R. Radhakrishnan, B. Uma, J. Liu, P. S. Ayyaswamy, D. M. Eckmann, Temporal multiscale approach for nanocarrier motion with simultaneous adhesion and hydrodynamic interactions in targeted drug delivery, Journal of computational physics 244 (2013) 252–263.

[15] T. Krüger, D. Holmes, P. V. Coveney, Deformability-based red blood cell separation in deterministic lateral displacement devicesa simulation study, Biomicrofluidics 8 (5) (2014) 054114.

[16] A. Yazdani, H. Li, J. D. Humphrey, G. E. Karniadakis, A general shear-dependent model for thrombus formation, PLoS Computational Biology 13 (1) (2017) e1005291.

[17] A. L. Fogelson, K. B. Neeves, Fluid mechanics of blood clot formation, Annual review of fluid mechanics 47 (2015) 377–403.

[18] H. Zhu, Z. Zhou, R. Yang, A. Yu, Discrete particle simulation of particulate systems: a review of major applications and findings, Chemical Engineering Science 63 (23) (2008) 5728–5770.

[19] C. Kloss, C. Goniva, A. Hager, S. Amberger, S. Pirker, Models, algorithms and validation for opensource dem and cfd–dem, Progress in Computational Fluid Dynamics, an International Journal 12 (2-3) (2012) 140–152.

[20] M. Chiesa, V. Mathiesen, J. A. Melheim, B. Halvorsen, Numerical simulation of particulate flow by the eulerian–lagrangian and the eulerian–eulerian approach with application to a fluidized bed, Computers & chemical engineering 29 (2) (2005) 291–304.

[21] J. B. Freund, The flow of red blood cells through a narrow spleen-like slit, Physics of Fluids (1994-present) 25 (11) (2013) 110807.

[22] C. Pozrikidis, Effect of membrane bending stiffness on the deformation of capsules in simple shear flow, Journal of Fluid Mechanics 440 (2001) 269–291.

[23] H. Zhao, E. S. Shaqfeh, V. Narsimhan, Shear-induced particle migration and margination in a cellular suspension, Physics of Fluids (1994-present) 24 (1) (2012) 011902.

[24] J. Donea, S. Giuliani, J.-P. Halleux, An arbitrary lagrangian-eulerian finite element method for transient dynamic fluid-structure interactions, Computer methods in applied mechanics and engineering 33 (1-3) (1982) 689–723.

[25] M. Souli, A. Ouahsine, L. Lewin, Ale formulation for fluid–structure interaction problems, Computer methods in applied mechanics and engineering 190 (5) (2000) 659–675.

[26] C. S. Peskin, The immersed boundary method, Acta numerica 11 (2002) 479–517.

[27] R. Mittal, G. Iaccarino, Immersed boundary methods, Annu. Rev. Fluid Mech. 37 (2005) 239–261.

[28] E. Constant, C. Li, J. Favier, M. Meldi, P. Meliga, E. Serre, Implementation of a discrete immersed boundary method in openfoam, arXiv preprint arXiv:1609.04364.

[29] R. Sun, H. Xiao, Sedifoam: A general-purpose, open-source cfd–dem solver for particle-laden flow with emphasis on sediment transport, Computers & Geosciences 89 (2016) 207–219.

[30] I. A. Cosden, J. R. Lukes, A hybrid atomistic–continuum model for fluid flow using lammps and openfoam, Computer Physics Communications 184 (8) (2013) 1958–1965.

[31] A. Peters, S. Melchionna, E. Kaxiras, J. Lätt, J. Sircar, M. Bernaschi, M. Bison, S. Succi, Multiscale simulation of cardiovascular flows on the ibm bluegene/p: Full heart-circulation system at red-blood cell resolution, in: Proceedings of the 2010 ACM/IEEE international conference for high performance computing, networking, storage and analysis, IEEE Computer Society, 2010, pp. 1–10.

[32] J. R. Clausen, D. A. Reasor, C. K. Aidun, Parallel performance of a lattice-boltzmann/finite element cellular blood flow solver on the ibm blue gene/p architecture, Computer Physics Communications 181 (6) (2010) 1013–1020.

[33] B. E. Griffith, Immersed boundary model of aortic heart valve dynamics with physiological driving and loading conditions, International Journal for Numerical Methods in Biomedical Engineering 28 (3) (2012) 317–345.

[34] S. C. Shadden, M. Astorino, J.-F. Gerbeau, Computational analysis of an aortic valve jet with lagrangian coherent structures, Chaos: An Interdisciplinary Journal of Nonlinear Science 20 (1) (2010) 017512.

[35] S. C. Shadden, A. Arzani, Lagrangian postprocessing of computational hemodynamics, Annals of biomedical engineering 43 (1) (2015) 41–58.

[36] D. Rossinelli, Y.-H. Tang, K. Lykov, D. Alexeev, M. Bernaschi, P. Hadjidoukas, M. Bisson, W. Joubert, C. Conti, G. Karniadakis, et al., The in-silico lab-on-a-chip: petascale and high-throughput simulations of microfluidics at cell resolution, in: Proceedings of the International Conference for High Performance Computing, Networking, Storage and Analysis, ACM, 2015, p. 2.

[37] P. Perdikaris, L. Grinberg, G. E. Karniadakis, Multiscale modeling and simulation of brain blood flow, Physics of Fluids (1994-present) 28 (2) (2016) 021304.

[38] B. E. Griffith, R. D. Hornung, D. M. McQueen, C. S. Peskin, An adaptive, formally second order accurate version of the immersed boundary method, Journal of Computational Physics 223 (1) (2007) 10–49.

[39] C. A. Taylor, T. J. Hughes, C. K. Zarins, Finite element modeling of blood flow in arteries, Computer methods in applied mechanics and engineering 158 (1) (1998) 155–196.

[40] A. Updegrove, N. M. Wilson, J. Merkow, H. Lan, A. L. Marsden, S. C. Shadden, Simvascular: An open source pipeline for cardiovascular simulation, Annals of Biomedical Engineering (2016) 1–17.

[41] P. Seil, S. Pirker, Lbdemcoupling: Open-source power for fluid-particle systems, in: Proceedings of the 7th International Conference on Discrete Element Methods, Springer, 2017, pp. 679–686.

[42] L. Peng, K.-i. Nomura, T. Oyakawa, R. K. Kalia, A. Nakano, P. Vashishta, Parallel lattice boltzmann flow simulation on emerging multi-core platforms, in: European Conference on Parallel Processing, Springer, 2008, pp. 763–777.

[43] E. S. Boek, M. Venturoli, Lattice-boltzmann studies of fluid flow in porous media with realistic rock geometries, Computers & Mathematics with Applications 59 (7) (2010) 2305–2314.

[44] M. A. Spaid, F. R. Phelan Jr, Lattice boltzmann methods for modeling microscale flow in fibrous porous media, Physics of fluids 9 (9) (1997) 2468–2474.

[45] X. He, S. Chen, R. Zhang, A lattice boltzmann scheme for incompressible multiphase flow and its application in simulation of rayleigh–taylor instability, Journal of Computational Physics 152 (2) (1999) 642–663.

[46] X. Shan, H. Chen, Lattice boltzmann model for simulating flows with multiple phases and components, Physical Review E 47 (3) (1993) 1815.

[47] J. Latt, Hydrodynamic limit of lattice boltzmann equations, Ph.D. thesis, University of Geneva (2007).

[48] J. Latt, Palabos, parallel lattice boltzmann solver (2009).

[49] S. Plimpton, Fast parallel algorithms for short-range molecular dynamics, Journal of computational physics 117 (1) (1995) 1–19.

[50] J. Zhang, P. C. Johnson, A. S. Popel, Red blood cell aggregation and dissociation in shear flows simulated by lattice boltzmann method, Journal of biomechanics 41 (1) (2008) 47–55.

[51] T. Krüger, F. Varnik, D. Raabe, Efficient and accurate simulations of deformable particles immersed in a fluid using a combined immersed boundary lattice boltzmann finite element method, Computers & Mathematics with Applications 61 (12) (2011) 3485–3505.

[52] R. M. MacMECCAN, J. Clausen, G. Neitzel, C. Aidun, Simulating deformable particle suspensions using a coupled lattice-boltzmann and finite-element method, Journal of Fluid Mechanics 618 (2009) 13–39.

[53] J. Tan, W. Keller, S. Sohrabi, J. Yang, Y. Liu, Characterization of nanoparticle dispersion in red blood cell suspension by the lattice boltzmann-immersed boundary method, Nanomaterials 6 (2) (2016) 30.

[54] S. Chen, G. D. Doolen, Lattice boltzmann method for fluid flows, Annual review of fluid mechanics 30 (1) (1998) 329–364.

[55] X. He, L.-S. Luo, Lattice boltzmann model for the incompressible navier–stokes equation, Journal of Statistical Physics 88 (3-4) (1997) 927–944.

[56] S. Succi, The lattice boltzmann equation for fluid dynamics and beyond, clarendon (2001).

[57] A. J. Ladd, Numerical simulations of particulate suspensions via a discretized boltzmann equation. part 1. theoretical foundation, Journal of Fluid Mechanics 271 (1994) 285–309.

[58] T. Inamuro, M. Yoshino, F. Ogino, Accuracy of the lattice boltzmann method for small knudsen number with finite reynolds number, Physics of Fluids (1994-present) 9 (11) (1997) 3535–3542.

[59] Y. Qian, D. d'Humières, P. Lallemand, Lattice bgk models for navier-stokes equation, EPL (Europhysics Letters) 17 (6) (1992) 479.

[60] Z. Guo, C. Zheng, B. Shi, Discrete lattice effects on the forcing term in the lattice boltzmann method, Physical Review E 65 (4) (2002) 046308.

[61] M. L. Parks, R. B. Lehoucq, S. J. Plimpton, S. A. Silling, Implementing peridynamics within a molecular dynamics code, Computer Physics Communications 179 (11) (2008) 777–783.

[62] S. A. Silling, Reformulation of elasticity theory for discontinuities and long-range forces, Journal of the Mechanics and Physics of Solids 48 (1) (2000) 175–209.

[63] J. Monaghan, R. Gingold, Shock simulation by the particle method sph, Journal of computational physics 52 (2) (1983) 374–389.

[64] J. J. Monaghan, Smoothed particle hydrodynamics, Annual review of astronomy and astrophysics 30 (1992) 543–574.

[65] R. D. Groot, P. B. Warren, et al., Dissipative particle dynamics: Bridging the gap between atomistic and mesoscopic simulation, Journal of Chemical Physics 107 (11) (1997) 4423.

[66] Y. Afshar, F. Schmid, A. Pishevar, S. Worley, Exploiting seeding of random number generators for efficient domain decomposition parallelization of dissipative particle dynamics, Computer Physics Communications 184 (4) (2013) 1119–1128.

[67] T. Ihle, D. Kroll, Stochastic rotation dynamics: a galilean-invariant mesoscopic model for fluid flow, Physical Review E 63 (2) (2001) 020201.

[68] S. Genheden, J. W. Essex, A simple and transferable all-atom/coarse-grained hybrid model to study membrane processes, Journal of chemical theory and computation 11 (10) (2015) 4749–4759.

[69] D. A. Fedosov, B. Caswell, G. E. Karniadakis, A multiscale red blood cell model with accurate mechanics, rheology, and dynamics, Biophysical journal 98 (10) (2010) 2215–2225.

[70] I. V. Pivkin, G. E. Karniadakis, Accurate coarse-grained modeling of red blood cells, Physical review letters 101 (11) (2008) 118105.

[71] D. A. Reasor, J. R. Clausen, C. K. Aidun, Coupling the lattice-boltzmann and spectrin-link methods for the direct numerical simulation of cellular blood flow, International Journal for Numerical Methods in Fluids 68 (6) (2012) 767–781.

[72] M. Dao, J. Li, S. Suresh, Molecularly based analysis of deformation of spectrin network and human erythrocyte, Materials Science and Engineering: C 26 (8) (2006) 1232–1244.

[73] D. A. Reasor Jr, M. Mehrabadi, D. N. Ku, C. K. Aidun, Determination of critical parameters in platelet margination, Annals of biomedical engineering 41 (2) (2013) 238–249.

[74] J. B. Freund, M. Orescanin, Cellular flow in a small blood vessel, Journal of Fluid Mechanics 671 (2011) 466–490.

[75] Z.-G. Feng, E. E. Michaelides, The immersed boundary-lattice boltzmann method for solving fluid–particles interaction problems, Journal of Computational Physics 195 (2) (2004) 602–628.

[76] Y. Liu, Y. Mori, Properties of discrete delta functions and local convergence of the immersed boundary method, SIAM Journal on Numerical Analysis 50 (6) (2012) 2986–3015.

[77] X. Yang, X. Zhang, Z. Li, G.-W. He, A smoothing technique for discrete delta functions with application to immersed boundary method in moving boundary simulations, Journal of Computational Physics 228 (20) (2009) 7821–7836.

[78] D. Goldstein, R. Handler, L. Sirovich, Modeling a no-slip flow boundary with an external force field, Journal of Computational Physics 105 (2) (1993) 354–366.

[79] J. Wu, C. K. Aidun, Simulating 3d deformable particle suspensions using lattice boltzmann method with discrete external boundary force, International journal for numerical methods in fluids 62 (7) (2010) 765–783.

[80] M.-C. Lai, C. S. Peskin, An immersed boundary method with formal second-order accuracy and reduced numerical viscosity, Journal of Computational Physics 160 (2) (2000) 705–719.

[81] G. B. Jeffery, The motion of ellipsoidal particles immersed in a viscous fluid, in: Proceedings of the Royal Society of London A: Mathematical, Physical and Engineering Sciences, Vol. 102, The Royal Society, 1922, pp. 161–179.

[82] L. Mountrakis, E. Lorenz, O. Malaspinas, S. Alowayyed, B. Chopard, A. G. Hoekstra, Parallel performance of an ib-lbm suspension simulation framework, Journal of Computational Science 9 (2015) 45–50.

[83] K. Müller, D. A. Fedosov, G. Gompper, Margination of micro-and nanoparticles in blood flow and its effect on drug delivery, Scientific reports 4.

[84] Y. Geng, P. Dalhaimer, S. Cai, R. Tsai, M. Tewari, T. Minko, D. E. Discher, Shape effects of filaments versus spherical particles in flow and drug delivery, Nature Nanotechnology 2 (4) (2007) 249–255.

[85] J. Boyle, Microcirculatory hematocrit and blood flow, Journal of theoretical biology 131 (2) (1988) 223–229.

[86] K. Vahidkhah, S. L. Diamond, P. Bagchi, Platelet dynamics in three-dimensional simulation of whole blood, Biophysical journal 106 (11) (2014) 2529–2540.

[87] L. M. Crowl, A. L. Fogelson, Computational model of whole blood exhibiting lateral platelet motion induced by red blood cells, International journal for numerical methods in biomedical engineering 26 (3-4) (2010) 471–487.

[88] M. Saadatmand, T. Ishikawa, N. Matsuki, M. Jafar Abdekhodaie, Y. Imai, H. Ueno, T. Yamaguchi, Fluid particle diffusion through high-hematocrit blood flow within a capillary tube, Journal of biomechanics 44 (1) (2011) 170–175.